Smart Agricultural Technology 14 (2026) 101754

Contents lists available at ScienceDirect

Smart Agricultural Technology

journal homepage: www.journals.elsevier.com/smart-agricultural-technology

# Leaf nitrogen content estimation in olive orchards based on analysis and modelling of UAV-acquired hyperspectral data

Daniel Argüello [a,*], Miguel Noguera [a], Federico Vaz [a], António Cordeiro [b], José Silvestre [b], Arturo Aquino [a]

[a] Centro de Investigación en Tecnología, Energía y Sostenibilidad (CITES), Universidad de Huelva, La Rábida, Palos de La Frontera, 21819 Huelva, España
[b] Instituto Nacional de Investigação Agrária e Veterinária, I.P. (INIAV), Herdade Do Reguengo, Elvas, Portugal

ARTICLE INFO

*Keywords:*
Nitrogen
Olive
Hyperspectral
Computer vision
Neural networks
Precision agriculture

ABSTRACT

Nitrogen (N) management is critical for optimising yield and quality in modern super high-density (SHD) olive orchards while minimising environmental impacts. Traditional leaf nitrogen content (LNC) assessment relies on costly and time-consuming laboratory methods, lacking the resolution for precision agriculture. This study evaluated the potential of unmanned aerial vehicle (UAV)-based hyperspectral sensing to non-invasively estimate LNC in SHD olive groves.Hyperspectral images (537 bands, 400–2500 nm) were acquired over an experimental orchard containing three olive varieties receiving contrasting N-fertigation treatments. Canopy spectral reflectance was extracted and subjected to preprocessing, including Savitzky-Golay filtering (first and second derivatives), scatter correction (MSC and SNV), and Principal Component Analysis (PCA). Partial Least Squares Regression (PLSR) and Artificial Neural Network (ANN) models were then trained to estimate LNC values derived from chemical analysis.

Results from an external validation set showed that the ANN model provided superior performance compared to PLSR. The best-performing ANN model, which utilised normalised information from both spectral derivatives, achieved outstanding predictive accuracy ($R^2 > 0.8$ and $RPD = 2.3$). This work demonstrates that a non-linear modelling approach leveraging UAV-acquired VNIR-SWIR hyperspectral data is a robust methodology for N status monitoring, offering the high spatial and temporal resolution required for precision fertilisation in modern olive cultivation.

## 1. Introduction

The global area under olive cultivation was about 11.1 Mha in 2023, with approximately 5 Mha located in the European Union (EU) and 2.7 Mha in Spain. Consequently, the EU accounted for 58 % of global production, with the main producing countries being Spain (25.1 %), Italy (11.8 %), Turkey (7.5 %), and Portugal (5.9 %). These figures highlight the importance of olive cultivation for the countries of the Mediterranean basin, where the olive sector serves as a key socio-economic engine.

In recent decades, the olive sector has undergone a transformation through the adoption of new cultivation systems, such as the super high-density (SHD) olive orchard. These crops are characterized by a continuous hedgerow structure, adapted to mechanized management tasks and high planting densities [1,2]. These features make olive cultivation more economically profitable, suggesting that SHD olive orchards are likely to become predominant in the future.

However, SHD olive orchards also present challenges, such as a higher demand for agricultural inputs and more complex agronomic management. For this reason, developing approaches to optimise SHD olive orchard management is crucial to ensure the viability and standardisation of this cultivation system within the sector [3].

One of the most relevant areas of agronomic management is fertilisation. The use of fertilisers significantly increases agricultural productivity and becomes indispensable in intensive cropping systems, where natural nutrient inputs cannot meet the crop's demands. Among the nutrients to be considered when designing a fertilisation plan, nitrogen (N) is of particular relevance due to its decisive impact on crop yield, growth and quality [4,5]. In SHD olive orchards, an overabundance of N tends to promote excessive vegetative development,

* Corresponding author.
*E-mail addresses:* daniel.arguello@pi.uhu.es (D. Argüello), miguel.noguera@diesia.uhu.es (M. Noguera), federico.vaz@pi.uhu.es (F. Vaz), antonio.cordeiro@iniav.pt (A. Cordeiro), jose.silvestre@iniav.pt (J. Silvestre), arturo.aquino@diesia.uhu.es (A. Aquino).

https://doi.org/10.1016/j.atech.2025.101754
Received 27 October 2025; Received in revised form 22 December 2025; Accepted 23 December 2025
Available online 24 December 2025
2772-3755/© 2025 Published by Elsevier B.V. This is an open access article under the CC BY-NC-ND license (http://creativecommons.org/licenses/by-nc-nd/4.0/).

which can adversely affect overall yield. Fruit production, closely linked to flowering intensity and fruit set, has been observed to rise with increasing foliar N levels between 0.8 % and 1.7 %, but declines when N surpasses this threshold [6]. While N fertilisation can enhance oil production, an excessive supply may compromise oil quality. One well-documented effect of surplus N is a reduction in total polyphenol content, which negatively impacts both the oxidative stability and bitterness of the oil [7]. Additionally, levels of monounsaturated fatty acids like oleic acid, valued for their health benefits, may decrease in proportion to polyunsaturated fatty acids [8]. On the other hand, excessive N application can have detrimental ecological consequences [9]. Therefore, the optimisation of N fertilisation strategies is critical to balancing crop productivity with environmental sustainability. This requires precise calibration of application rates based on specific nutritional requirements [10].

Traditionally, the main tool used to adjust fertilisers doses in SHD olive orchards is the leaf tissue analysis [11]. However, this method relies on laboratory-based analytical techniques, which are costly, laborious and time consuming, so they are restricted to a limited number of locations and time points. For these reasons, chemical methods lack the spatial and temporal resolution required for being applied in precision agriculture contexts.

This concern has aroused numerous research efforts focused on developing new methodologies to assess the N status of crops, with spectroscopy-based techniques being among the most prominent. These approaches rely on the principle that abnormal N levels in crops induce physiological and structural changes that alter their spectral reflectance properties. Accordingly, mathematical modelling tools can be used to establish correlations between the spectral reflectance of the canopy at specific wavelengths and the N status of vegetation [10]. Furthermore, in recent decades, advances in unmanned aerial vehicle (UAV) platforms and photogrammetry software have greatly expanded the potential of these methodologies. The main advantage of these systems lies in their ability to cover large field areas at low altitudes, enabling the acquisition of ultra-high-resolution images while minimising atmospheric interference [12].

One of the most critical aspects of imaging spectroscopy techniques for assessing the N status of vegetation is the modelling of spectral data. Approaches in this domain have evolved from simple empirical algorithms to advanced computational techniques. Initially, research focused on parametric regression based on Vegetation Indices (VIs), primarily targeting the chlorophyll response [13,14]. However, these methods are limited by unstable physiological correlations and fail to fully exploit the wealth of continuous spectral information, particularly in the SWIR domain associated with proteins [15].

To overcome these limitations, current trends favour non-parametric regression methods that analyse the full spectrum without predefined assumptions [16]. Within this category, linear techniques like Partial Least Squares Regression (PLSR) effectively reveal hidden multivariate patterns [17]. Nevertheless, non-linear Machine Learning (ML) models represent the most significant advancement, as they efficiently model non-linear relationships without requiring prior knowledge of the underlying data distribution, unlike their predecessors. Comparative studies confirm that ML frequently achieves higher estimation accuracy than linear and parametric techniques [18–21].

Although many studies have demonstrated the potential of spectroscopy techniques for estimating the N status of a several crops, only a limited number of works have focused on olive cultivation [10]. Existing studies in this domain can be categorized based on the measurement scale, ranging from laboratory analyses to ground-based and airborne assessments.

Regarding laboratory-based research, Rotbart et al. [22] evaluated different spectrometers and preprocessing methods for generating PLSR models, finding that thoroughly ground, dried leaves yielded the most accurate N assessments. In a similar vein, Comino et al. [23] proposed a multi-sensor approach combining NIR spectroscopy and Portable Energy Dispersive X-Ray Fluorescence. Their PLSR models, aimed at predicting multiple nutrients, achieved semi-quantitative estimates for N.

In terms of field-based measurements, several authors have investigated canopy reflectance using portable spectroradiometers. For example, Gómez-Casero et al. [24] analysed spectral curves in the VNIR region, developing a stepwise discriminant model that successfully classified trees subjected to different N fertilization levels. Furthermore, Rubio-Delgado et al. [25] evaluated the performance of various VIs and PLSR models using a full-range spectroradiometer (350–2500 nm). In their study, indices such as DCNI and TCARI exhibited the strongest relationships with Leaf Nitrogen Content (LNC), while PLSR also demonstrated good predictive potential.

Finally, to address spatial variability at the orchard scale, methodologies based on Unmanned Aerial Vehicles (UAV) have been explored. Noguera et al. [26] assessed N, P, and K levels using multispectral imagery (475–840 nm). They compared various linear and non-linear regression methods to develop predictive models, with Artificial Neural Networks (ANN) providing the best performance. However, the estimation results for LNC were modest, a limitation the authors attributed to the absence of spectral bands in the SWIR region.

This research aims to advance the state of the art in estimating the N status of olive crops, addressing the current gap in the application of airborne hyperspectral sensing to this sector. Specifically, we investigate the capabilities of a high-performance hyperspectral camera (537 bands, 400–2500 nm) for estimating the LNC of SHD olive groves. Unlike previous studies based on laboratory measurements or limited spectral ranges, this work leverages the full VNIR–SWIR spectrum acquired from a UAV platform, enabling efficient coverage of large crop areas while retaining very high spatial and spectral resolution. The proposed methodology involves analysing and modelling hyperspectral images to retrieve canopy spectral reflectance at specific locations. After applying different preprocessing techniques, the spectral data were used as predictors in ANN and PLSR models trained to estimate reference LNC values obtained through chemical analysis. The potential of this approach was evaluated in an experimental field trial involving three olive varieties subjected to contrasting N treatments, thereby providing a robust framework to assess the feasibility of hyperspectral UAV imagery for operational nutrient monitoring in modern olive production systems.

The remainder of this paper is organised as follows: Section 2 details the experimental framework design, the acquisition logistics, the processing of image and spectral data, and the models' development and testing. Section 3 provides an analysis and discussion of the obtained results. Section 4 concludes the study by presenting the main findings and sketching potential avenues for future research.

## 2. Materials and methods

### 2.1. Experimental design

#### 2.1.1. Study area

This study was conducted in an experimental olive orchard, provided by Bolschare Agriculture S.L., which was specifically managed to induce trees covering a wide spectrum of nutritional statuses. The orchard is located near Elvas, in the district of Portalegre (Alentejo, Portugal) (38°55′14.8″ N, 7°07′23.21″ W). This 4.8 ha site is arranged in a super high-density (SHD) planting system (4 $m$ × 1.35 m), and it is divided into three sectors cultivated with the Aceitera, Arbequina, and Koroneiki varieties, respectively.

The experimental protocol was applied to three olive varieties, establishing three distinct fertigation treatments to induce variability in crop nutritional status. Each treatment was assigned to an elemental plot consisting of five tree rows within each variety. The first treatment served as a control (Rainfed), where trees were maintained under rainfed conditions without supplemental water or fertilisation. The other two treatments involved fertigation using a drip irrigation system

equipped with emitters spaced at 1 m intervals (flow rate of 2.2 $L{\cdot}h^{-1}$), with an irrigation frequency of approximately 10 h per week. A ternary liquid fertiliser (12–2–8 N-P-K) was applied starting on March 9th. The second treatment (Standard) followed a commercial recommendation, providing total annual inputs of 90 kg N $ha^{-1}$, 15 kg $P_2O_5$ $ha^{-1}$, and 60 kg $K_2O$ $ha^{-1}$. The third treatment (High N) involved doubling these doses to 180 kg N $ha^{-1}$, 30 kg $P_2O_5$ $ha^{-1}$, and 120 kg $K_2O$ $ha^{-1}$. Regarding the temporal distribution of inputs, approximately 80 % of the total scheduled nitrogen had been supplied by the first week of June, ensuring that nutritional differences were well-established before the image acquisition campaign.

Within the treated area, 67 sampling points were selected and geo-referenced for each variety, resulting in a total of 201 points. For each variety, 33 points were located in the area subjected to the standard fertigation treatment, while 17 points were placed in each of the areas subjected to nutrient deficiency and excess treatments, respectively. The sampling points were placed in the central row, leaving two rows on each side as treatment controls. These points serve as objective references for assessing the nutritional status of the olive trees.

#### 2.1.2. Plant material and reference analysis

In this research, leaf nitrogen content (LNC) was selected as the target parameter. LNC is a mass-based metric expressing the amount of N in crop tissue (usually leaves or biomass) as a percentage of the total dry matter. It is commonly reported in units such as [mg/g] or [ %]. The characterisation of this parameter at key stages of the vegetative cycle is widely used as a reference for N status in commercial olive orchards, supporting the implementation of amendments in fertigation programs [11].

On the same day as the flight mission, foliar samples were collected from each of the previously geo-referenced sampling points ($n = 201$). Each sampling unit consisted of 100 $\pm$ 20 g of leaves harvested from spring terminal shoots. The samples were placed in plastic bags and refrigerated for transport to the laboratory, where they were analysed by chemical methods.

LNC determination was carried out using the Kjeldahl method. Leaf samples were washed with distilled water, dried at 65 $\pm$ 5°C, and ground to a particle size of 1 $\pm$ 0.1 mm. Then, 500 mg of ground material was digested in tubes containing Kjeldahl catalyst tablets and 10 ml of concentrated sulfuric acid, converting N compounds into ammonium sulphate. The digestion block temperature program consisted of 30 min at 185 °C followed by 60 min at 410 °C. After digestion, 50 ml of 40 % sodium hydroxide was added, and the released ammonium was distilled as ammonia. The ammonia was condensed in a cooling system and collected in a conical flask containing 20 ml of 2 % boric acid solution. Finally, the solution was titrated with 0.025 M hydrochloric acid to quantify the ammonia content.

### 2.2. Equipment

The hyperspectral sensing system used in this study was a Headwall Hyperspec Co-Aligned VNIR-SWIR camera (Headwall Photonics, Bolton, Massachusetts, USA), designed specifically for airborne applications. This system consists of two co-aligned push-broom sensors operating simultaneously in the VNIR and SWIR spectral ranges, providing a total of 537 spectral bands readings. The VNIR sensor collects 273 spectral bands, covering the 399–1002.8 nm range, with a band width of approximately 2.2 nm. In contrast, the SWIR sensor acquires 270 spectral bands, extending from 899.4–2509.2 nm, and features a band width of about 6 nm. As a push-broom (line-scanning) system, it captures one spatial dimension of 640 pixels and the full spectral signature per line, while the second spatial dimension, $m$, is reconstructed through continuous motion along the flight direction [27]. These features result in the generation of two three-dimensional hyperspectral data cubes, one per sensor, of dimensions $m \times 640 \times b$, where $b$ denotes the number of bands sampled for the considered sensor. The hyperspectral sensing system used in this study was a Headwall Hyperspec Co-Aligned VNIR-SWIR camera (Headwall Photonics, Bolton, Massachusetts, USA), designed specifically for airborne applications. This system consists of two co-aligned push-broom sensors operating simultaneously in the VNIR and SWIR spectral ranges, providing a total of 537 spectral bands readings. The VNIR sensor collects 273 spectral bands, covering the 399–1002.8 nm range, with a band width of approximately 2.2 nm. In contrast, the SWIR sensor acquires 270 spectral bands, extending from 899.4–2509.2 nm, and features a band width of about 6 nm. As a push-broom (line-scanning) system, it captures one spatial dimension of 640 pixels and the full spectral signature per line, while the second spatial dimension, $m$, is reconstructed through continuous motion along the flight direction [27]. These features result in the generation of two three-dimensional hyperspectral data cubes, one per sensor, of dimensions $m \times 640 \times b$, where $b$ denotes the number of bands sampled for the considered sensor.The system features a compact design (272 mm $\times$ 208 mm $\times$165 mm) and moderate weight ($\sim$ 4 kg), making it suitable for unmanned aerial vehicle (UAV) integration. Data acquisition and system configuration were managed via HyperSpec III (Headwall Photonics, Bolton, Massachusetts, USA), the manufacturer's proprietary software, which also performed radiometric calibration and mission planning. Table 1 summarises the camera-related key features described above.

To carry the hyperspectral system, a DJI Matrice 600 Pro (DJI, Shenzhen, China) multirotor UAV was used (see Fig. 1). This professional grade hexacopter provides high payload capacity, flight stability, and modular integration capability for scientific instrumentation. With an operational weight of $\sim$ 10 kg and a maximum take-off weight (MTOW) of 15.5 kg, the UAV is powered by six TB48D batteries, delivering a maximum flight autonomy of approximately 18 min under full load conditions. The Camera's GNSS-RTK module, coupled with onboard IMU, enabled precise geo-referencing of the captured imagery. Check Table 2 for a summary of the UAV's main features.

### 2.3. Flight planning

To completely map the approximately 3 ha experimental plot, three independent flights were conducted. This multi-flight approach was necessary to ensure full spatial continuity without compromising data quality or operational safety. To guarantee consistent overlap between adjacent flight lines and preserve the integrity of the spectral information captured by the push-broom sensor, a lateral overlap of 50% was established between flight paths, minimising potential data loss due to positional drift or in-flight instability.

Each flight consisted of two clearly defined phases. The first phase, conducted manually, included takeoff, initialisation and stabilisation of the real-time kinematic positioning system (RTK-GPS), and landing. The second phase, corresponding to the autonomous data acquisition, was executed using the photogrammetry mission planning tool embedded in UgCS (SPH Engineering, Riga, Latvia), This software enabled the precise

**Table 1**
Technical specifications of the Headwall Hyperspec co-aligned VNIR-SWIR camera.

| Parameter | VNIR Module | SWIR Module |
|---|---|---|
| Spectral range (nm) | 399–1002.8 | 899.4–2509.2 |
| Spectral bands | 273 | 270 |
| Band width (nm) | ~2.2 | ~6 |
| Spatial resolution (pixels) | 640 | 640 |
| Sensor technology | CMOS | Stirling-cooled Mercury Cadmium Telluride (MCT) |
| Dimensions (mm) | 272 × 208 × 165 | |
| Weight (kg) | ~4 | |
| Acquisition mode | Push-broom | Push-broom |
| Software | HyperSpec III | HyperSpec III |
| Positioning system | GNSS-RTK + IMU | |


**Fig. 1.** DJI Matrice 600 Pro UAV equipped with Headwall Hyperspec Co-Aligned VNIR-SWIR hyperspectral camera.

**Table 2**
Technical specifications of the DJI matrice 600 Pro UAV.

| Parameter | Value |
|---|---|
| UAV type | Multirotor (hexacopter) |
| Max Takeoff Weight (MTOW) (kg) | 15.5 |
| Operational weight (with payload) (kg) | ~10 |
| Max flight time (with payload) (min) | ~18 |
| Battery configuration | 6 × TB48D |
| Max speed (km/h) | ~65 |
| Positioning system | GPS + IMU |

definition of capture polygons and the automated execution of optimised flight trajectories over the target area at a constant altitude of 90 m above ground level (AGL). A visual example of a programmed flight polygon in UgCS is shown in Fig. 2.

Flight speed parameters were determined prior to each mission based on the prevailing ambient light conditions. To minimize the presence of cast shadows and self-shading within the canopy, data acquisitions were scheduled near solar noon. Specifically, flights were conducted exclusively under stable illumination scenarios either completely cloud-free skies or uniform overcast conditions to avoid irradiance fluctuations caused by moving clouds during data acquisition. A white reference surface exposed to direct sunlight, in combination with the diagnostic and exposure calibration tools available in HyperSpec III, was used to adjust the integration time of the sensor, optimising acquisition speed and ensuring that no pixels were overexposed or underexposed.

**Fig. 2.** 3D illustration of the flight mission plan over the experimental olive grove, as planned in the UgCS software interface. The green lines indicate the drone's flight path.

In addition, a calibrated spectralon reflectance panel was placed within the defined capture polygons to facilitate the transformation of raw digital values into absolute reflectance during image processing. The polygon coordinates were uploaded to the hyperspectral camera through HyperSpec III, enabling the onboard system using high-precision RTK-GPS to recognise in real time when the UAV entered the target sampling zone. This enabled selective acquisition, ensuring that hyperspectral data were only recorded over predefined areas of interest, thus avoiding the collection of extraneous or non-relevant information.

### 2.4. Generation and filtering sample points' canopy spectra

#### 2.4.1. Image preprocessing

The preprocessing of hyperspectral images was carried out using the proprietary software HyperSpec III, which provides an integrated workflow for spectral normalisation, radiometric correction, and orthorectification, each being essential to ensure the quality, comparability, and geospatial accuracy of the acquired data [28].

The first step involved radiometric correction. This was performed using a "dark frame" reference image acquired immediately prior to each flight. This image, captured with the sensor shutter closed, eliminates thermal and electronic noise inherent to the sensor by establishing a baseline radiance level per pixel. This correction ensures that the observed spectral variations in the imagery are attributable solely to the true reflectance properties of the targets, and not to instrument-related artifacts [29].

Subsequently, reflectance correction was applied using a calibrated reflectance panel (spectralon, Headwall Photonics, Bolton, Massachusetts, USA) of 3 × 3m, composed of three regions with distinct and certified reflectance coefficients. This panel was placed within the flight capture area and was used as an absolute reference target. The spectral values recorded over this surface enabled the transformation of radiance-corrected data into spectrally normalised apparent reflectance

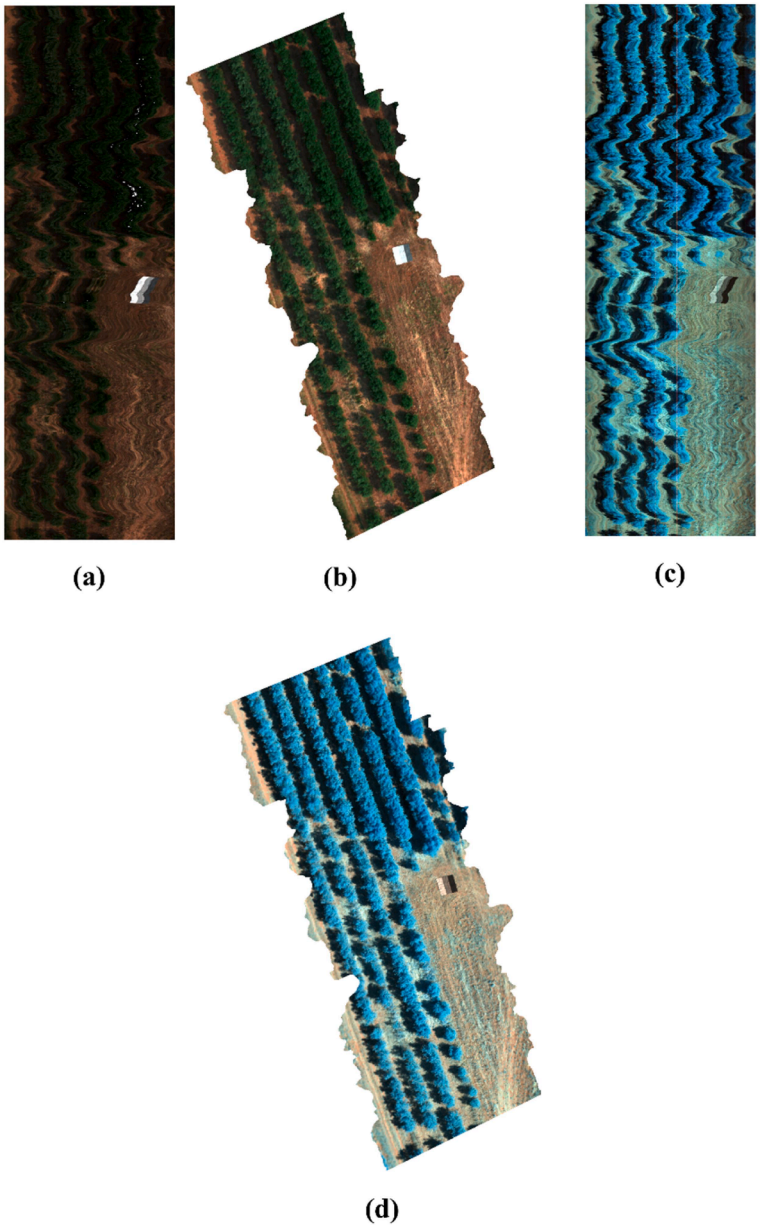


**Fig. 3.** Comparison of multispectral aerial images from a portion of the sampling area before and after radiometric and orthogonal correction. (a) Uncorrected VNIR image. (b) VNIR image with radiance, reflectance, and orthogonal corrections. (c) Uncorrected SWIR image. (d) SWIR image with radiance, reflectance, and orthogonal corrections.

values. This correction is critical for maintaining consistency across different flight sessions, as it mitigates errors associated with variations in ambient illumination caused by changes in solar angle, cloud cover, or atmospheric conditions throughout the day [30].

Finally, orthorectification was performed to geo-reference and project the images into real-world coordinates, compensating for geometric distortions caused by UAV motion during flight. This process relied on data from the inertial measurement unit (IMU) embedded in the sensor, which records angular rotations and accelerations in real time, combined with GNSS positions acquired via RTK. These datasets were processed using POSPac UAV software (Applanix Corporation, Richmond Hill, Ontario, Canada) to generate a Smoothed Best Estimate of Trajectory (SBET) file, providing a highly accurate and temporally synchronised estimation of the sensor's trajectory, including position, speed, and orientation [28]. To generate the SBET file, raw GNSS data were downloaded from a local base station in Spain (code: BADJ) files for the days of data collection with a frequency of 1 s. In addition, a Digital Elevation Model (DEM), encoded in the WGS84 coordinate system, was required to complete the orthorectification process.

Fig. 3 illustrates the result of the described process for radiometric and orthogonal correction.

### 2.4.2. Extraction of representative spectral information from reference points

Once the radiometric, reflectance, and orthorectification corrections described above were completed, the extraction of spectral information associated with the field-defined sampling specimens was performed. However, following the geo-referencing process, a slight spatial mismatch was observed between the original GPS coordinates assigned to the sampling points and the actual canopy positions of the olive trees in the hyperspectral imagery. This discrepancy is attributed to the intrinsic limitations of the GPS accuracy embedded in the sensor, as well as the complexity of the orthorectification process in UAV-based push-broom systems, where small deviations in trajectory data or DEM alignment can propagate into positional shifts in the final orthomosaic. As a result, a spatial offset occurred between the expected sampling windows and the actual location of the tree crowns.

To address this discrepancy, a custom software tool was developed to visualize the geo-referenced hyperspectral images and overlay the original GPS positions of the sampling points. This tool enabled the manual repositioning of the spectral sampling windows, defined as square patches of 11×11 pixels, onto the corresponding tree canopies. Each sample was individually adjusted using high-resolution satellite imagery as a visual reference, ensuring that all pixels within each window were confined exclusively to the olive tree canopy under study, thus avoiding the inclusion of non-representative elements such as soil, cast shadows, surrounding vegetation, while minimizing the influence of woody branches due to the high leaf density characteristic of SHD hedgerows.

After correcting and validating the positions of all sampling windows, spectral data were extracted. For each window (121 pixels per sample), the mean spectral value for each band was calculated across all pixels within the window. This averaging approach was adopted to obtain a representative spectral signature of the canopy. As a result of this process, a mean spectral signature was obtained for each sample and sampling session, consisting of a $1 \times 273$ vector for the VNIR region and a $1 \times 270$ vector for the SWIR region, where the second dimension corresponds to the reflectance values recorded by each sensor across the spectral bands (see illustration in Fig. 4). Mathematically:

$$VNIR_i = \left(v_i^1, \ldots, v_i^{273}\right), \; SWIR_i = \left(s_i^1, \ldots, s_i^{270}\right),$$

such that $v_i^j$ and $s_i^k$ are the average reflectance values from the $j$-th and $k$-th bands within the VNIR and SWIR regions, respectively, for the $i = 1, \ldots, 804$ records resulting from sampling the 201 selected olive tree specimens across the four sampling sessions.

### 2.4.3. Spectral bands filtering

As a first step, the spectral bands in $VNIR_i$ corresponding to wavelengths between 898.4–1002.8 nm were discarded to avoid duplicity, as they were also present in $SWIR_i$. Subsequently, a systematic removal of spectral bands in $SWIR_i$ that exhibited a low signal-to-noise ratio (SNR) was carried out. This resulted in the discard of bands corresponding to 1336.2–1432 nm and 1803–2509 nm.

The removal of the 1336.2–1432 nm band is standard practice, as it directly corresponds to a strong atmospheric $H_2O$ vapour absorption band centred at approximately 1400 nm [31].

The justification for excluding the broader 1829.3–2509.2 nm range is multifactorial. Firstly, a dominant and broad water vapour absorption

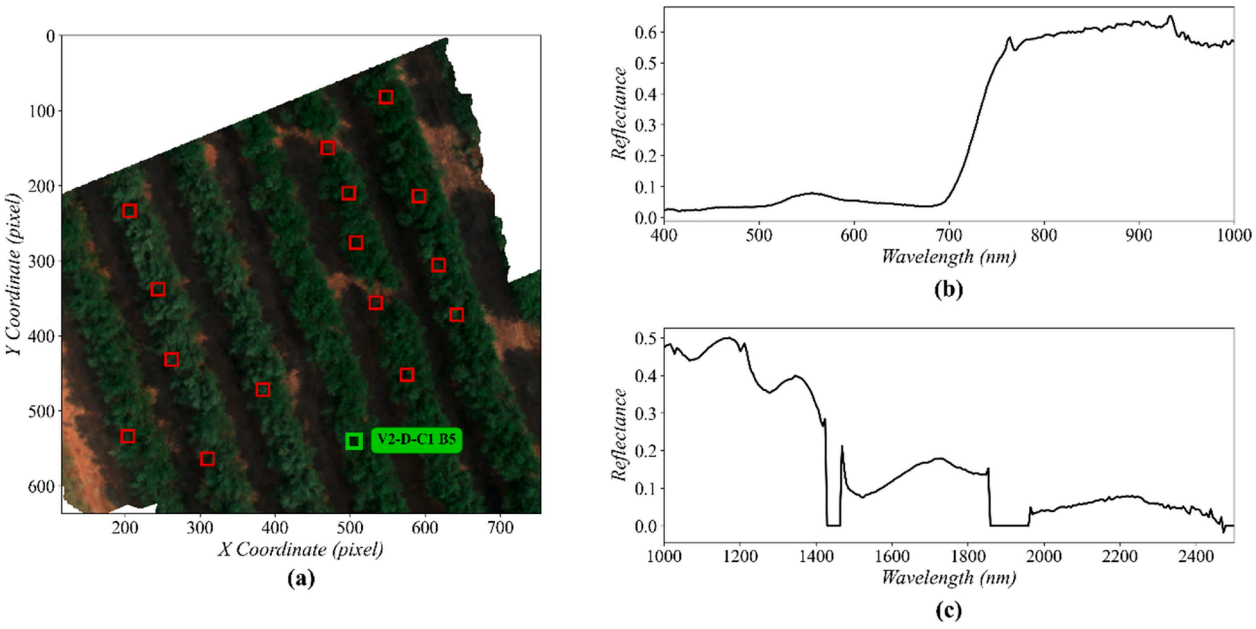


**Fig. 4.** Spectral signature extraction from an olive tree canopy. (a) Illustration of 121-pixel (11×11) window used for spectral characterisation of sample V2-D-CI B5. (b) Mean VNIR spectral reflectance profile. (c) Mean SWIR spectral reflectance profile.

band is also present around 1900 nm [31]. However, data quality degradation extends well beyond this specific feature. Besides atmospheric effects, fundamental physical constraints reduce the SNR at these longer wavelengths. Indeed, solar irradiance naturally decreases significantly in this portion of the spectrum, meaning fewer photons reach the Earth's surface and, consequently, the sensor by reflection. Moreover, as the wavelength approaches the sensor's operational limit, the quantum efficiency of its MCT photodetectors becomes inherently lower, and they produce more thermal noise than at shorter wavelengths [32]. These combined physical principles result in a substantially lower SNR. In addition, this spectral segment also contains another significant atmospheric absorption feature, dominated by $H_2O$ and $CO_2$, which becomes prominent beyond 2450 nm [31], further compromising signal integrity.

Because of the justified bands filtering, $VNIR_i$ and $SWIR_i$ vectors' dimensionality is reduced according to the following definitions:

$$VNIR_{i,f} = \left(v_i^1, \ldots, v_i^{225}\right),\ SWIR_{i,f} = \left(s_i^1, \ldots, s_i^{134}\right),$$

being the vectors then concatenated to form a set of vectors $V_i$ comprising all the filtered spectral information:

$$F_i = \left(v_i^1, \ldots, v_i^{225}, s_i^1, \ldots, s_i^{134}\right) = \left(f_i^1, \ldots, f_i^{359}\right)$$

### 2.5. Spectral data preprocessing

Spectral preprocessing is a common step that aims to smooth noise and correct signal defects such as light scattering that it is inherent to spectral acquisitions [33]. In the case of aerial systems operating in the field under uncontrolled illumination conditions, signal noise and degradation is especially a prominent concern [34].

Three widely used preprocessing approaches were applied in this study: 1) spectral smoothing and derivation, and outlier filtering; 2) scatter-corrective methods; 3) spectral dimensionality reduction. Given the previously commented noisy nature of the spectral signals of this study, smoothing and derivation, as well as outliers filtering, was applied prior to scattering corrections to prevent derivatives from amplifying noise components. Thus, the following workflow was applied to improve spectral information as a previous step to estimation model development:

- Smoothing and derivation, and outlier filtering: the spectra were processed using a Savitzky-Golay (SG) filter [35] to smooth noise and subsequently compute its first and second derivatives. The first derivative allows to remove the baseline, whereas the second corrects both the baseline and linear trend [33]. Following an empirical evaluation, a 9-point window size and a second-order polynomial were selected. This combination was determined to provide an optimal trade-off, achieving effective noise reduction while preserving the integrity and intrinsic shape of key absorption bands. Thus, given an $i$-th $F_i$ spectral vector, the smoothed vector $F_{i,SG}$, and the first and second derivative vectors $F'_{i,SG}$ and $F''_{i,SG}$, are given by:

$$F_{i,SG}, F'_{i,SG}, F''_{i,SG} = SG(F_i,\ o = 2,\ w = 9)$$

were $o$ and $w$ denote the polynomial order and window size, respectively.

Outlier detection was then performed using the interquartile range (IQR) method, which is defined as the difference between the 75th percentile (Q3) and the 25th percentile (Q1) [36]. Spectral vectors were classified as outliers if at least one band fell below the lower fence, specified as $Q1 - 1.5 \times IQR$, or above the upper fence, designated as $Q3 + 1.5 \times IQR$. Identified outliers were subsequently removed from the analysis after corroborating they were mainly attributable to image sensors failures, or partial and temporary cloudiness during the data acquisition flight. Outlier filtering yielded as result 551 validated $F_{i,SG}, F'_{i,SG}$ and $F''_{i,SG}$ vectors.

Fig. 5 shows the smoothed and filtered VNIR and SWIR spectra, along with their first and second derivatives.

- Scatter correction: Multiplicative Scatter Correction (MSC) was applied to remove, from the first derivative, multiplicative variance arising from light scattering. This approach favours that the resulting spectra are primarily shaped by the chemical absorption features of interest [37]. This procedure corrects for global scatter differences among samples by aligning each spectrum to a common reference, which was calculated as the mean of all $F'_{i,SG}$ spectra. Mathematically, the set of corrected derived spectra, $V'_{MSC,m-M}$, is calculated by applying MSC followed by min-max normalisation, according to:

$$V'_{MSC,m-M} = \left\{ \frac{VR'_{i,MSC} - \min\left(V'_{MSC}\right)}{\max\left(V'_{MSC}\right) - \min\left(V'_{MSC}\right)} \middle| i = 1, \ldots, 551 \right\},\ \text{such that}$$

$$V'_{MSC} = \left\{ VR'_{i,MSC} \middle| i = 1, \ldots, 551 \right\},\ \text{and}$$

$$VR'_{i,MSC} = \frac{F'_{i,SG} - b_i}{a_i},$$

where the coefficients $a_i$ (slope) and $b_i$ (offset) are obtained from a least-squares linear regression of spectrum $F'_{i,SG}$ against the reference spectrum $S_{ref}$ as:

$$F'_{i,SG} \approx a_i \times S_{ref} + b_i,$$

The reference spectral vector, $S_{ref}$, is computed as the average of all $n = 551$ sample spectral vectors as:

$$S_{ref} = \frac{1}{n} \times \sum_{j=1}^{n} F'_{j,SG}$$

The correction of light-scattering multiplicative variance effects present in the second derivative was addressed by applying the Standard Normal Variate (SNV) transformation [38] (see Fig. 6). This procedure normalises each spectrum individually by centring it to a mean of zero and scaling it to unit standard deviation. Mathematically, the set of min-max corrected and normalised second derivative spectra, $V''_{SNV,m-M}$, is obtained by applying:

$$V''_{SNV,m-M} = \left\{ \frac{VR''_{i,SNV} - \min\left(V''_{SNV}\right)}{\max\left(V''_{SNV}\right) - \min\left(V''_{SNV}\right)} \middle| i = 1, \ldots, 551 \right\},\ \text{such that}$$

$$V''_{SNV} = \left\{ VR''_{i,SNV} \middle| i = 1, \ldots, 551 \right\},\ \text{and}$$

$$VR''_{i,SNV} = \frac{F''_{i,SG} - \mu\left(F''_{i,SG}\right)}{\sigma\left(F''_{i,SG}\right)},$$

where $\mu$ and $\sigma$ denote the average and standard deviation values, respectively.

Fig. 6 provides a representation of the normalised VNIR and SWIR first and second derivatives.

- Spectral dimensionality reduction: high-dimensional spectral data inherently suffer from the curse of high dimensionality and strong multicollinearity, where adjacent spectral variables are highly correlated. To overcome these difficulties, Principal Component Analysis (PCA) was employed to simplify the feature space by reducing dimensionality of spectral vectors, which mitigates multicollinearity, enhances computational efficiency, and favours

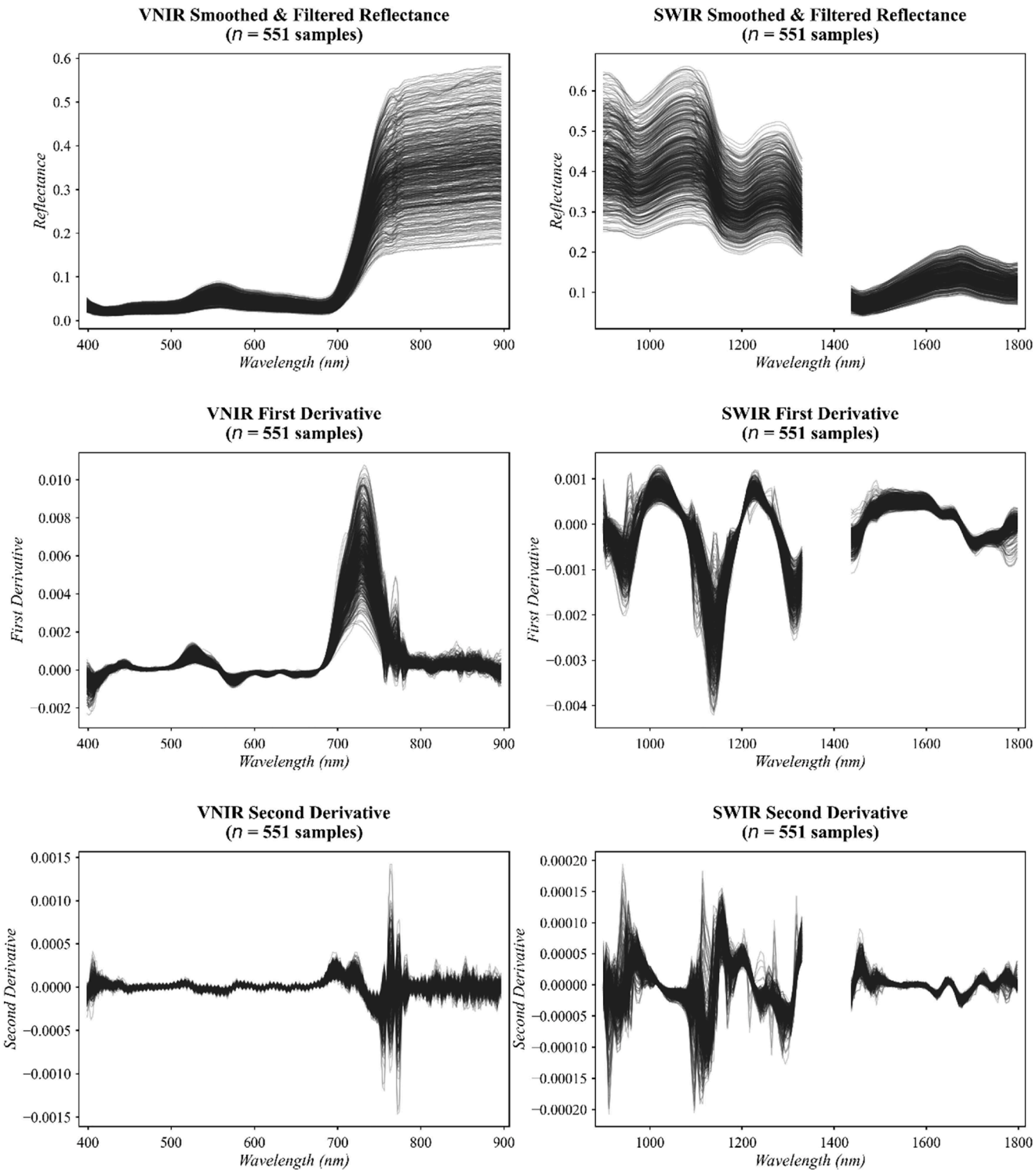


**Fig. 5.** Smoothed and filtered spectral dataset ($n = 551$ samples). The left column displays data from the VNIR sensor (400–900 nm), and the right column displays data from the SWIR sensor (950–1800 nm). Rows correspond to: (Top) Smoothed and filtered reflectance spectra; (Middle) First derivative spectra; and (Bottom) Second derivative spectra.

obtaining more robust and generalisable models [39]. Concretely, PCA was applied on the sets $V'_{MSC,m-M}$ and $V''_{SNV,m-M}$ as follows:

$$P' = \mathrm{PCA}(V'_{\mathrm{MSC},m-M}$$

$$P'' = \mathrm{PCA}\left(V''_{\mathrm{NSV},m-M}\right), \text{ such that}$$

$$P' = \left\{PR'_i \middle| i = 1, \ldots, 551\right\} \text{ and}$$

$$P'' = \left\{PR''_i \middle| i = 1, \ldots, 551\right\},$$

The number of principal components configuring the transformed

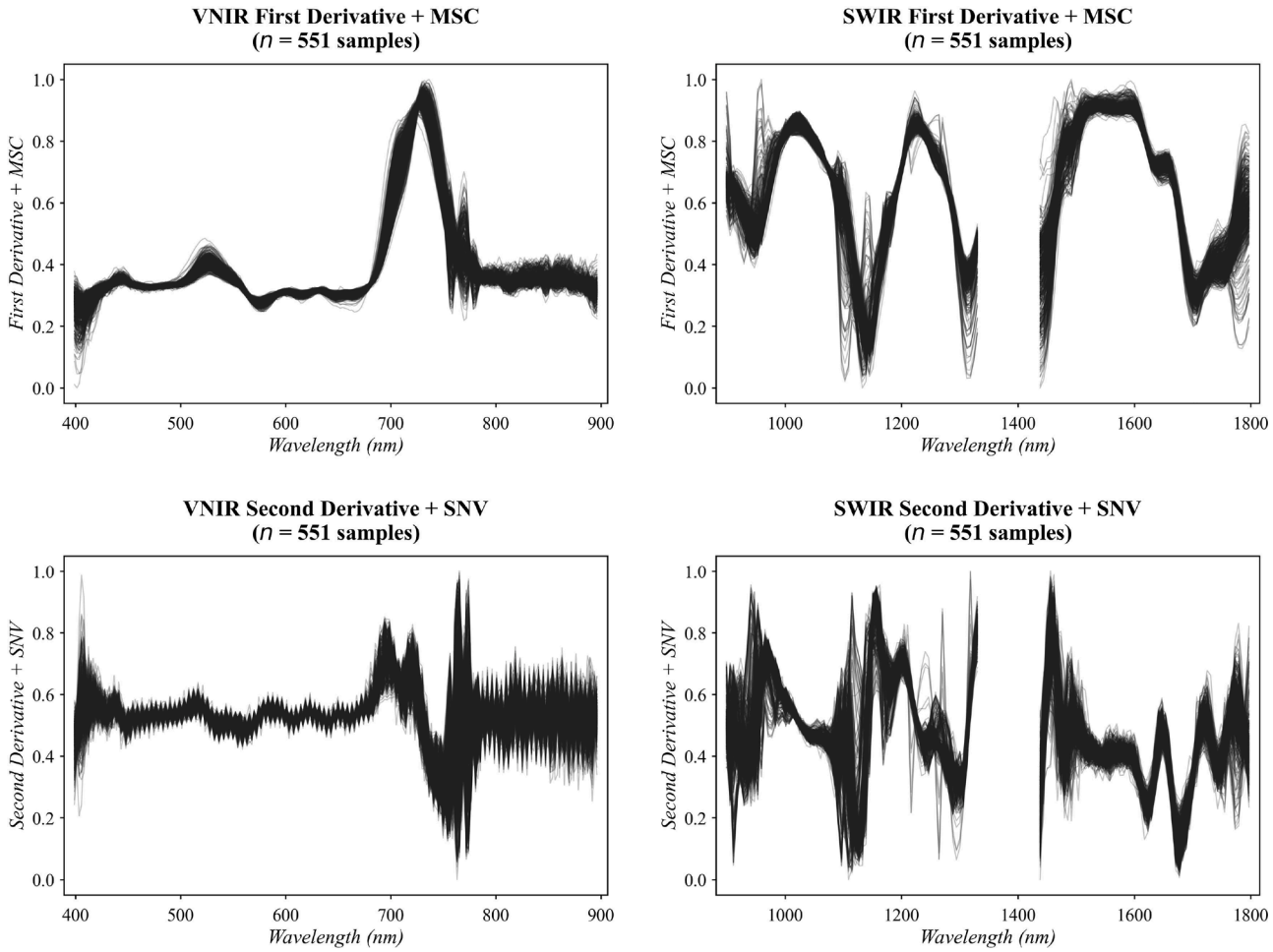


**Fig. 6.** Scatter-corrected derivative spectra ($n = 551$ samples). The top row displays the first derivative spectra normalised using MSC. The bottom row displays the second derivative spectra normalised using SNV. Left and right columns correspond to the VNIR and SWIR spectral ranges, respectively.

vectors $PR_i'$ and $PR_i''$ was that required to keep at least 95% of variance of the original feature spaces. Concretely:

$$\mathrm{PR}_i' = \left(\mathrm{pr}_i'^{\,1},\ \ldots, \mathrm{pr}_i'^{\,14}\right)$$

$$\mathrm{PR}_i'' = \left(\mathrm{pr}_i''^{\,1},\ \ldots, \mathrm{pr}_i''^{\,44}\right)$$

The definitive sample vectors used for subsequent modelling, $SLNC_i$, are those resulting from the concatenation of $PR_i'$ and $PR_i''$:

$$SLNC_i = \left(pr_i'^{\,1},\ \ldots, pr_i'^{\,14}, pr_i''^{\,1},\ \ldots, pr_i''^{\,44}\right) = \left(slnc_i^1,\ \ldots, slnc_i^{60}\right)$$

### 2.6. Datasets configuration, and estimation model training

Leaf nitrogen content (LNC) is the target variable to be estimated from the spectral information contained in the $SLNC_i$ vectors. Thus, consider a dataset of 551 elements consisting of $LNC_i$ values, determined by chemical analysis as described in Section 2.1.2, and their corresponding $SLNC_i$ vectors. Prior to model development, this dataset was divided into training (90%, $n = 500$) and external validation sets (10%, $n = 51$). To preserve the underlying data distribution, a k-Nearest Neighbours (k-NN) algorithm was first applied using the scalar $LNC_i$ values to group observations into 10 clusters. Within each cluster, samples were then systematically assigned to the two subsets according to their $LNC_i$ values, with extreme $LNC_i$ values being explicitly allocated to the training set. This procedure ensured that the variance of the training set remained comparable to that of the external validation set (see Fig. 7). The training and external validation sets were employed to train, test and compare the performance of two models: partial least square regression (PLSR), and artificial neural network (ANN).

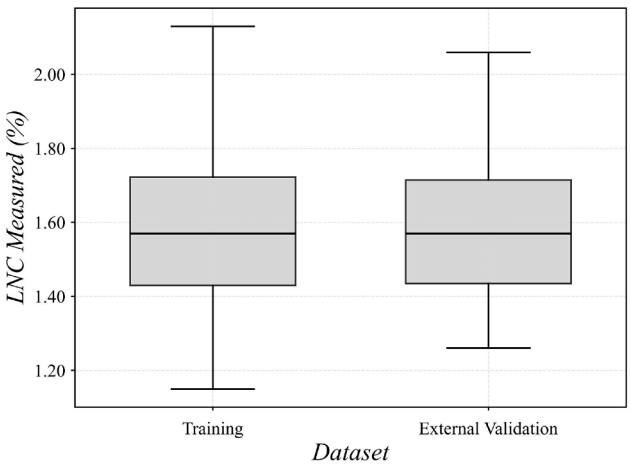


**Fig. 7.** Box plot distribution of the measured Leaf Nitrogen Content (LNC) ( %) for the training and external validation datasets.

PLSR is a linear, non-parametric regression method based on the generation of latent variables maximising covariance between predictors and responses. It is achieved while reducing issues of overfitting by converting correlated variables into a smaller set of independent

factors. This approach not only decreases data dimensionality but also uncovers key structures that account for variability in both predictors and responses. It is particularly advantageous for predicting outcomes from highly interrelated predictors or in cases where the number of predictors surpasses the number of observations [40]. In agricultural research, PLSR has proven especially useful for exploring the connections between multiple N indicators and vegetation indices (VIs) [17].

ANNs fall within the category of non-parametric regression techniques. They are able to model complex non-linear relationships between predictors without requiring prior knowledge of the underlying data distribution. This capability gives ANNs greater flexibility to capture the intricate non-linear interactions that often occur between vegetation spectral signatures and their biophysical traits, representing a methodological advantage over linear approaches. Comparative studies have shown that non-parametric regression techniques, including ANNs, frequently achieve greater estimation accuracy than linear techniques [18–21]. The ANN used in this study was a fully connected feedforward multilayer perceptron, which was structured as follows: 1) an input layer with 60 neurons, corresponding to the 60 elements of $SLNC_i$ vectors; 2) a hidden layer with 10 neurons; 3) an output layer with a single neuron to yield LNC estimations. $LNC_i$ values associated to $SLNC_i$ vectors were used as output for the network's fitting. A hyperbolic tangent sigmoid transfer function was selected from among others, as it was found to favour proper network fitting.

### 2.7. Methodology for performance evaluation

The ability of the trained models to estimate leaf nitrogen content (LNC) was evaluated on the external validation set of $n = 51$ sample points using three metrics.

On the one hand, a linear correlation study was carried out by confronting the actual and the predicted LNC values. The outcomes of this study were assessed by calculating Pearson's coefficient of determination, $R^2$.

The root-mean-square-error (RMSE) between the reference LNC values obtained by chemical analysis and the responses of each model was calculated as:

$$RMSE = \sqrt{\frac{\sum_{i=1}^{n}(\widehat{LNC}_i - LNC_i)^2}{n}}$$

where, for the $i$-th sample, $LNC_i$ is the actual LNC value determined by chemical analysis, and $\widehat{LNC}_i$ is the LNC value predicted by the models.

Finally, the ratio of performance to deviation (RPD) was also considered and computed as the ratio between the standard deviation ($\sigma$) of LNC reference values, and the RMSE:

$$RPD = \frac{\sigma(LNC_i)}{RMSE}$$

RPD is a metric that evaluates a model's predictive ability by comparing the standard deviation of the reference data to the standard error of prediction. In terms of interpretation, models where $RPD < 1.5$ are generally considered unsuitable for practical applications. If $1.5 \leq RPD < 2.0$, the model is deemed capable of distinguishing between high and low values, making it adequate for rough screening. A model exhibits very good predictive performance when $RPD > 2.0$, and this performance is considered excellent when $RPD > 3.0$ [41,42].

## 3. Results and discussion

Table 3 summarises the results obtained with the artificial neural network (ANN) and partial least square regression (PLSR) models, both evaluated on the external validation set ($n = 51$). The first and second columns show the results derived from providing the models with normalised information exclusively from the 1st or the 2nd derivative, respectively. The third column provides the results obtained by feeding the models with normalised information from both derivatives as it is described in Sections 2.5. and 2.6. PLSR and ANN models fed with one derivative information exclusively registered analogous performance. However, the inclusion of information from both derivatives led to a marked improvement especially in the ANN's performance, outstandingly achieving correlation coefficients ($R^2$) greater than 0.8 and RPD values approaching 2.3 (check Fig. 8). In contrast, the corresponding performance gain for the PLSR model was significantly more modest. These results suggest that a non-linear combination of the two descriptor sets may be the optimal approach to fully exploit the information contained within the datasets.

**Table 3**
Comparative performance of ANN and PLSR models on the external validation set ($n = 51$), using first and second derivative preprocessing with MSC and SNV normalisation.

| | 1st deriv. + MSC $n = 51$ | | 2nd deriv. + SNV $n = 51$ | | 1st deriv. + MSC, 2nd deriv. + SNV $n = 51$ | |
|---|---|---|---|---|---|---|
| | ANN | PLSR | ANN | PLSR | ANN | PLSR |
| *RMSE* ( %) | 0.10 | 0.10 | 0.10 | 0.10 | 0.09 | 0.09 |
| *RPD* | 2.07 | 2.07 | 2.01 | 2.08 | 2.29 | 2.1392 |
| $R^2$ | 0.7616 | 0.7655 | 0.7495 | 0.7648 | 0.8062 | 0.7771 |

Most research employing spectroscopy to determine nitrogen (N) status of crops has focused primarily on grasses such as wheat, rice, and maize [11]. In contrast, studies targeting olive trees remain relatively limited.

In this sense, Robart et al. [24] assessed the feasibility of estimating LNC of olives using VIS–NIR spectroscopy under laboratory conditions. Their study compared the performance of PLSR models built from spectra of intact leaves with those developed from dried and ground samples. The best predictive performance ($R^2 = 0.91$; $RPD = 3.32$) was achieved using the first derivative of absorbance spectra obtained from finely ground, dried leaves within the 1100–2500 nm range. These results contrasted sharply with those derived from intact leaves ($R^2 = 0.57$). The authors attributed this difference to two main factors: the enhanced sample homogeneity resulting from grinding, and the removal of water-related absorption peaks that could mask N-specific spectral features in fresh leaves.

In a related study, Comino et al. [25] explored the combined use of NIR spectroscopy (1000–2500 nm) and portable energy-dispersive X-ray fluorescence (EDXRF) for determining LNC and other elemental concentrations in ground and dried olive leaves. Using PLSR, they compared models developed from each technique individually and from the integration of both datasets. For N estimation, the best performance was achieved using NIR spectroscopy alone ($R^2 = 0.73$; $RPD = 1.8$), whereas combining NIR and EDXRF data reduced model accuracy.

The results obtained in the aforementioned studies are comparable to those obtained in the present research. This highlights the performance achieved by the developed estimation models, particularly considering that the spectral predictors were obtained directly in the field through non-invasive measurements.

Other authors have also examined non-invasive approaches for assessing N status of olive trees based on field-acquired spectral data. Gómez-Casero et al. [26], proposed a discriminant analysis approach to classify olive trees subjected to different N fertilisation regimes. Spectral data were collected with a spectroradiometer (400–900 nm) positioned above the tree canopy using a telescopic pole. Both individual spectral bands and vegetation indices were used as predictors to build discriminant models, achieving classification accuracies ranging from 62.5% to 99.2%. The authors concluded that the spectral signature of olive canopies is influenced by their N status, particularly within the 710–900 nm region.

More recently, Rubio Delgado et al. [27] evaluated several vegetation indices (VIs) and PLSR models using different combinations of spectral bands and preprocessing techniques to predict olive LNC.

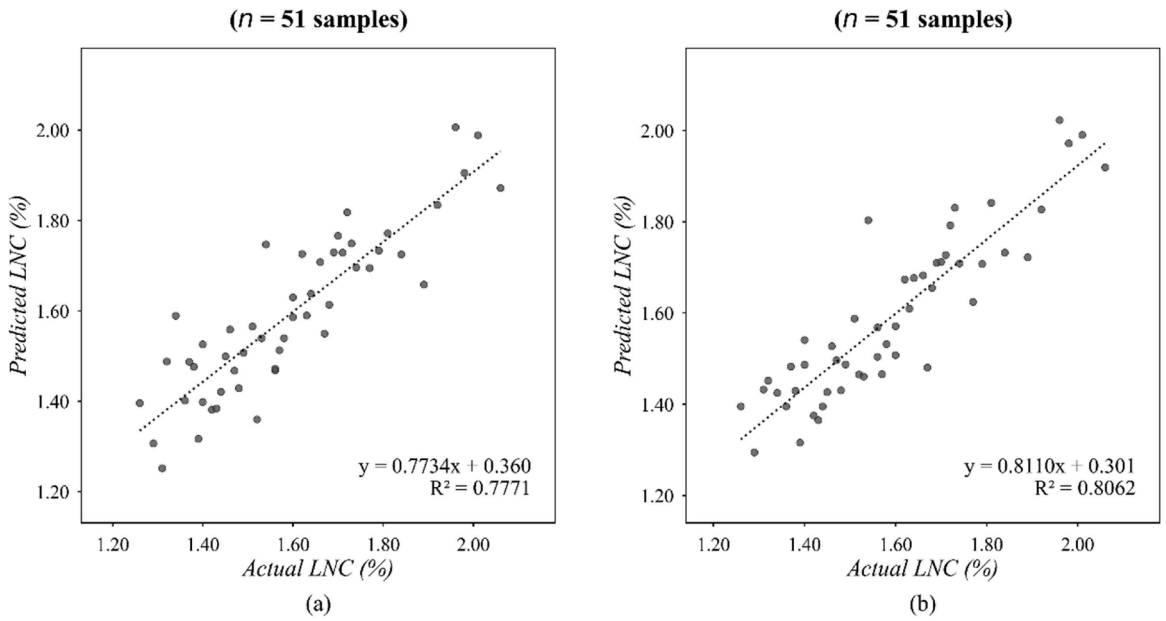


**Fig. 8.** Scatter plots of actual vs. predicted Leaf Nitrogen Content (LNC) for the external validation dataset ($n = 51$). Results are shown for (a) the PLSR model and (b) the ANN model.

Spectral reflectance was recorded with a handheld spectroradiometer (350–2500 nm) from stacks of leaves placed on the ground under direct sunlight. Among the tested VIs, DCNI and TCARI exhibited the strongest relationships with LNC ($R^2 = 0.72$ and $R^2 = 0.64$, respectively). The PLSR model achieved $R^2 = 0.56$ under fivefold cross-validation. Both methods performed best when the predictor variables were preprocessed using the second derivative combined with Multiplicative Scatter Correction (SNV) transformation.

The methodology proposed in the present work offers clear technical advantages over these previous approaches. Our framework is based on in vivo hyperspectral imagery acquired in the field from a nadir perspective using an unmanned aerial vehicle (UAV). This setup introduces new challenges—particularly in terms of image calibration and data variability—that are effectively addressed through the proposed image processing pipeline. Once processed, these images encompass the entire crop area, enabling the extraction of spectral information from every tree in a fully non-invasive manner. As a result, the proposed methodology provides an unprecedented level of spatial resolution compared to earlier studies centred on olive crop. Moreover, the use of UAVs allows for the monitoring of extensive cultivation areas with minimal human effort. In practical terms, this capability could facilitate more frequent sampling, thereby enhancing the temporal resolution of N monitoring in olive groves.

Despite these additional challenges, the models developed in this study outperform those reported in previous works. This improvement is likely attributable to the inclusion of both spectral derivatives as input features and, in the case of the ANN-based model, to its ability to capture nonlinear relationships between spectral and biochemical variables.

It is also worth noting that some of the authors of the present work previously proposed a similar methodology based on the analysis and modelling of multispectral images (475–840 nm) for predicting olive LNC. That earlier study also evaluated different modelling strategies, with the ANN-based approach again yielding the best results ($R^2 = 0.63$). However, the predictive performance was more modest than in the current research [28]. This difference can likely be attributed to the superior capabilities of the hyperspectral sensor used here, which captures a greater number of narrower bands across a considerably broader spectral range, resulting in a more detailed and informative spectral signature. Consequently, the inclusion of NIR and SWIR bands likely enhances the model's ability to capture the variability associated with LNC. Furthermore, the model developed in this study demonstrates improved generalisation capacity, as it was trained and validated on data collected across multiple phenological stages of three different olive varieties.

Finally, regarding the economic feasibility, while the high cost of the full-range hyperspectral sensor limits its direct commercial implementation, its use is fundamental for research. It allows for the identification of optimal spectral features, which is a prerequisite for the development of future cost-effective sensors tailored for the olive industry.

## 4. Conclusion

Nitrogen (N) is a key determinant when designing fertilisation strategies, given its critical impact on crop yield, overall growth, and quality. However, the overuse of N leads to environmental damage. Consequently, continuous, accurate, and objective monitoring of the plant's N status across all phenological stages is vital to enhance N use efficiency.

This paper presents a study aimed at exploring the potential of modelling Leaf Nitrogen Content (LNC) from hyperspectral information acquired in a commercial olive grove using a UAV-based sensing platform. Unlike previous studies based on laboratory measurements or limited spectral ranges, LNC estimation is addressed by leveraging the full VNIR–SWIR spectrum (400–2500 nm), captured under real-world illumination conditions and throughout an entire olive growing season.

The acquired hyperspectral data from reference individuals were processed and subsequently used to train, externally validate, and compare the performance of partial least squares regression (PLSR) and artificial neural network (ANN) models. The best performance for both models was achieved when utilising normalised information from the first and second derivatives of the processed spectral records. Nevertheless, the ANN model's performance was superior, achieving outstanding coefficients of determination ($R^2$) greater than 0.8 and RPD values approaching 2.3, which suggests an optimal combination of spectral information is achieved by employing a non-linear approach.

This work represents a significant contribution to the state of the art in the non-invasive monitoring of N status in the super high-density (SHD) olive orchard. Basing the proposed methodology on the analysis and modelling of aerial imagery confers an unprecedented spatial and

temporal resolution for this crop. Additionally, having trained and validated the estimation models with data from multiple phenological stages and olive varieties strengthens their generalisation capacity, thereby lending greater robustness to the results achieved.

From the perspective of future commercial implementation, the methodology proposed in this research suggests promising operational advantages over the traditional paradigm. The capability to monitor LNC with high spatial and temporal resolution offers the potential to adjust fertilization rates to the specific requirements of each orchard zone throughout the phenological cycle. In the long term, this could translate into economic savings derived from input optimization, which, coupled with improved production efficiency, would enhance farm profitability. Furthermore, the further development and consolidation of these tools would significantly expand the understanding of N uptake dynamics in SHD olive orchards and their interaction with biotic and abiotic factors, paving the way for more precise management strategies.

Future work will focus on re-evaluating the developed models with data of successive campaigns. Furthermore, the proposed methodology will be evaluated with additional olive tree varieties and phenological development stages. Finally, we will seek to expand this methodology toward the determination of other nutrients of interest for olive orchard fertilisation management. In parallel, future work will also address the generation of high-resolution spatial distribution maps of LNC at the orchard scale. This development will require overcoming specific technical challenges associated with push-broom sensors, particularly the precise orthorectification and mosaicking of individual flight lines to reconstruct the full scene, followed by the implementation of robust canopy segmentation algorithms to isolate tree reflectance from soil background.

## Funding

This work was supported by: Grant CNS2022_136,137 funded by MICIU/AEI/10.13039/501,100,011,033 and by “European Union NextGenerationEU/PRTR”; the Interreg Cooperation Program VI-A SPAIN-PORTUGAL (POCTEP) 2021–27 and co-financed with ERDF, grant number 0067_OLIVARIA_5_E, within the scope of the OlivarIA Project.

## Declaration of generative AI use

During the preparation of this work the authors used Gemini in order to improve language and readability of the manuscript. After using this tool/service, the authors reviewed and edited the content as needed and takes full responsibility for the content of the published article.

## Ethical statement

The authors declare that the article does not involve studies with humans or animals.

## CRediT authorship contribution statement

**Daniel Argüello:** Writing – review & editing, Writing – original draft, Visualization, Validation, Software, Resources, Methodology, Investigation, Formal analysis, Data curation, Conceptualization. **Miguel Noguera:** Writing – review & editing, Writing – original draft, Visualization, Validation, Resources, Methodology, Investigation, Data curation, Conceptualization. **Federico Vaz:** Validation, Software, Investigation, Formal analysis. **António Cordeiro:** Methodology, Data curation, Conceptualization. **José Silvestre:** Methodology, Investigation, Data curation, Conceptualization. **Arturo Aquino:** Writing – review & editing, Writing – original draft, Visualization, Validation, Supervision, Software, Resources, Project administration, Methodology, Investigation, Funding acquisition, Formal analysis, Data curation, Conceptualization.

## Declaration of competing interest

The authors declare that they have no known competing financial interests or personal relationships that could have appeared to influence the work reported in this paper.

## Data availability

Data will be made available on request.

## References

[1] D.J. Connor, M. Gómez-del-Campo, M.C. Rousseaux, P.S. Searles, Structure, management and productivity of hedgerow olive orchards: a review, Sci. Hortic 169 (2014) 71–93, https://doi.org/10.1016/J.SCIENTA.2014.02.010. Apr.

[2] R. Lo Bianco, P. Proietti, L. Regni, T. Caruso, Planting systems for modern olive growing: strengths and weaknesses, Agriculture 11 (6) (2021) 494, https://doi.org/10.3390/AGRICULTURE11060494, 2021. Vol,. 11. Page. 494May.

[3] E. Roma, P. Catania, Precision oliviculture: research topics, challenges, and opportunities—a review, Remote. Sens. 14 (7) (2022) 1668, https://doi.org/10.3390/rs14071668. Mar.

[4] R. Erel, A. Dag, A. Ben-Gal, A. Schwartz, U. Yermiyahu, Flowering and fruit set of olive trees in response to nitrogen, phosphorus, and potassium, J. Am. Soc. Hortic. Sci. 133 (5) (2008) 639–647, https://doi.org/10.21273/jashs.133.5.639. Sep.

[5] A. Haberman, et al., Significance of proper nitrogen fertilization for olive productivity in intensive cultivation, Sci. Hortic 246 (2019) 710–717, https://doi.org/10.1016/J.SCIENTA.2018.11.055. Feb.

[6] R. Erel, U. Yermiyahu, J. Van Opstal, A. Ben-Gal, A. Schwartz, A. Dag, The importance of olive (Olea europaea L.) tree nutritional status on its productivity, Sci. Hortic 159 (2013) 8–18, https://doi.org/10.1016/J.SCIENTA.2013.04.036. Jul.

[7] R. Fernández-Escobar, G. Beltrán, M.A. Sánchez-Zamora, J. García-Novelo, M. P. Aguilera, M. Uceda, Olive oil quality decreases with nitrogen over-fertilization, HortScience 41 (1) (2006) 215–219, https://doi.org/10.21273/hortsci.41.1.215. Feb.

[8] A. Dag, et al., Olive oil composition as a function of nitrogen, phosphorus and potassium plant nutrition, J. Sci. Food. Agric 89 (11) (2009) 1871–1878, https://doi.org/10.1002/JSFA.3664. Aug.

[9] I. Rashmi, et al., Organic and inorganic fertilizer contaminants in agriculture: impact on soil and water resources. Contaminants in Agriculture: Sources, Impacts and Management, Springer, Cham, 2020, pp. 3–41, https://doi.org/10.1007/978-3-030-41552-5_1.

[10] K. Berger, et al., Crop nitrogen monitoring: recent progress and principal developments in the context of imaging spectroscopy missions, Remote. Sens. Env. 242 (2020) 111758, https://doi.org/10.1016/j.rse.2020.111758. Jun.

[11] L. Barranco Navero, Fernandez Escobar Diego, Rallo Romero Ricardo, El Cultivo Del Olivo, 7a ed, Mundi-Prensa Libros, Madrid, 2017.

[12] D. Li, et al., Application of unmanned aerial vehicle optical remote sensing in crop nitrogen diagnosis: a systematic literature review, Comput. Electron. Agric 227 (2024) 109565, https://doi.org/10.1016/J.COMPAG.2024.109565. Dec.

[13] P. Chen, D. Haboudane, N. Tremblay, J. Wang, P. Vigneault, B. Li, New spectral indicator assessing the efficiency of crop nitrogen treatment in corn and wheat, Remote. Sens. Env. 114 (9) (2010) 1987–1997, https://doi.org/10.1016/J.RSE.2010.04.006. Sep.

[14] A.M. Ali, H.M. Salem, Site-specific nitrogen fertilizer management using canopy reflectance sensors, chlorophyll meters and leaf color charts: a review, Nitrogen 5 (4) (2024) 828–856, https://doi.org/10.3390/NITROGEN5040054, 2024. Vol,. 5. Pages. 828-856Sep.

[15] J. Dai, et al., A general methodology for the quantification of crop canopy nitrogen across diverse species using airborne imaging spectroscopy, Remote. Sens. Env. 298 (2023) 113836, https://doi.org/10.1016/J.RSE.2023.113836. Dec.

[16] J. Verrelst, et al., Quantifying vegetation biophysical variables from imaging spectroscopy data: a review on retrieval methods, Surv. Geophys 40 (3) (2019) 589–629, https://doi.org/10.1007/s10712-018-9478-y. May.

[17] P.M. Hansen, J.K. Schjoerring, Reflectance measurement of canopy biomass and nitrogen status in wheat crops using normalized difference vegetation indices and partial least squares regression, Remote. Sens. Env. 86 (4) (2003) 542–553, https://doi.org/10.1016/S0034-4257(03)00131-7. Aug.

[18] P. Miphokasap, W. Wannasiri, Estimations of nitrogen concentration in sugarcane using hyperspectral imagery, Sustainability 10 (4) (2018) 1266, https://doi.org/10.3390/su10041266. Apr.

[19] X. Yao, et al., Evaluation of six algorithms to monitor wheat leaf nitrogen concentration, Remote. Sens. 7 (11) (2015) 14939–14966, https://doi.org/10.3390/rs71114939. Nov.

[20] Q. Yi, J. Huang, F. Wang, X. Wang, Evaluating the performance of PC-ANN for the estimation of rice nitrogen concentration from canopy hyperspectral reflectance, Int. J. Remote. Sens 31 (4) (2010) 931–940, https://doi.org/10.1080/01431160902912061.

[21] L. Liang, et al., Estimation of leaf nitrogen content in wheat using new hyperspectral indices and a random forest regression algorithm, Remote. Sens. 10 (12) (2018) 1940, https://doi.org/10.3390/RS10121940, 2018. Vol,. 10. Page. 1940Dec.

[22] N. Rotbart, et al., Estimating olive leaf nitrogen concentration using visible and near-infrared spectral reflectance, Biosyst. Eng 114 (4) (2013) 426–434, https://doi.org/10.1016/j.biosystemseng.2012.09.005. Apr.
[23] F. Comino, M.J. Ayora-Cañada, V. Aranda, A. Díaz, A. Domínguez-Vidal, Near-infrared spectroscopy and X-ray fluorescence data fusion for olive leaf analysis and crop nutritional status determination, Talanta 188 (2018) 676–684, https://doi.org/10.1016/j.talanta.2018.06.058. Oct.
[24] M.T. Gómez-Casero, F. López-Granados, J.M. Peña-Barragán, M. Jurado-Expósito, L. García-Torres, R. Fernández-Escobar, Assessing nitrogen and potassium deficiencies in olive orchards through discriminant analysis of hyperspectral data, J. Am. Soc. Hortic. Sci. 132 (5) (2007) 611–618, https://doi.org/10.21273/jashs.132.5.611. Sep.
[25] J. Rubio-Delgado, et al., Predicting leaf nitrogen content in olive trees using hyperspectral data for precision agriculture, Precis. Agric 22 (1) (2020) 1–21, https://doi.org/10.1007/s11119-020-09727-1. Feb.
[26] M. Noguera, et al., Nutritional status assessment of olive crops by means of the analysis and modelling of multispectral images taken with UAVs, Biosyst. Eng 211 (2021) 1–18, https://doi.org/10.1016/j.biosystemseng.2021.08.035. Nov.
[27] R.I. Hartley, R. Gupta, Linear pushbroom cameras, in: J.-O. Eklundh (Ed.), Lecture Notes in Computer Sciences. Computer Vision — ECCV '94, Springer-Verlag, Stockholm, 1994, pp. 555–564.
[28] S. Jakob, R. Zimmermann, R. Gloaguen, The need for accurate geometric and radiometric corrections of drone-borne hyperspectral data for mineral exploration: mEPHySTo—A toolbox for pre-processing drone-borne hyperspectral data, Remote. Sens. 9 (1) (2017) 88, https://doi.org/10.3390/RS9010088. Jan.
[29] H.S. Shin, S.H. Go, J.H. Park, Robust radiometric and geometric correction methods for drone-based hyperspectral imaging in agricultural applications, Korean. J. Remote. Sens. 40 (3) (2024) 257–268, https://doi.org/10.7780/KJRS.2024.40.3.2. Jun.
[30] R.D. Jackson, M. Susan Moran, P.N. Slater, S.F. Biggar, Field calibration of reference reflectance panels, Remote. Sens. Env. 22 (1) (1987) 145–158, https://doi.org/10.1016/0034-4257(87)90032-0. Jun.
[31] R.N. Clark, Chapter 1: spectroscopy of rocks and minerals, and principles of spectroscopy, in: A.N. Rencz (Ed.), Manual of Remote Sensing, Volume 3: Remote Sensing For the Earth Sciences, John Wiley & Sons, Ltd, 1999, pp. 3–58.
[32] J.R. Schott, Remote Sensing: The Image, the Science, and the Technology, Oxford University Press, 2007.
[33] Å. Rinnan, F. van den Berg, S.B. Engelsen, Review of the most common pre-processing techniques for near-infrared spectra, TrAC. Trends. Anal. Chem. 28 (10) (2009) 1201–1222, https://doi.org/10.1016/J.TRAC.2009.07.007. Nov.
[34] T. Adão, et al., Hyperspectral Imaging: a review on UAV-based sensors, data processing and applications for agriculture and forestry, Remote. Sens. 9 (11) (2017) 1110, https://doi.org/10.3390/RS9111110, 2017. Vol,. 9. Page. 1110Oct.
[35] A. Savitzky, M.J.E. Golay, Smoothing and differentiation of data by simplified least squares procedures, Anal. Chem 36 (8) (1964) 1627–1639.
[36] J.W. Tukey, Exploratory Data Analysis, Addison-Wesley Publishing Company, 1977 vol. 2.
[37] T. Isaksson, T. Naes, The effect of multiplicative scatter correction (MSC) and linearity improvement in NIR spectroscopy, Appl. Spectrosc 42 (7) (1988) 1273–1284, https://doi.org/10.1366/0003702884429869.
[38] R.J. Barnes, M.S. Dhanoa, S.J. Lister, Standard normal variate transformation and de-trending of near-infrared diffuse reflectance spectra, Appl. Spectrosc 43 (5) (1989) 772–777, https://doi.org/10.1366/0003702894202201.
[39] I.T. Jolliffe, Principal Component Analysis, 2nd ed., Elsevier, Berlin, Heidelberg, 2002.
[40] S. Wold, M. Sjöström, L. Eriksson, PLS-regression: a basic tool of chemometrics, Chemom. Intell. Lab. Syst. 58 (2) (2001) 109–130, https://doi.org/10.1016/S0169-7439(01)00155-1. Oct.
[41] B.M. Nicolaï, et al., Nondestructive measurement of fruit and vegetable quality by means of NIR spectroscopy: a review, Postharvest. Biol. Technol 46 (2) (2007) 99–118, https://doi.org/10.1016/J.POSTHARVBIO.2007.06.024. Nov.
[42] S. Marín-San Román, M.P. Diago, J. Fernández-Novales, C. Cebrián-Tarancón, M. R. Salinas, T. Cerdán-Garde, Use of the hyperspectral imaging to estimate the volatile composition of Tempranillo grape berries during ripening, Sci. Hortic 337 (2024) 113537, https://doi.org/10.1016/J.SCIENTA.2024.113537. Nov.